



**HAL**  
open science

## Modified 4-Point Bending Test for Adhesion Measurement at the Interface of Iron Coated with Aluminum Casting Alloy

M. Zhe, O. Dezellus, G. Parry, M. Braccini, J.C. Viala

► **To cite this version:**

M. Zhe, O. Dezellus, G. Parry, M. Braccini, J.C. Viala. Modified 4-Point Bending Test for Adhesion Measurement at the Interface of Iron Coated with Aluminum Casting Alloy. *Journal of Adhesion Science and Technology*, 2012, 26, pp.1-17. 10.1163/016942411X559049 . hal-00802010

**HAL Id: hal-00802010**

**<https://hal.science/hal-00802010>**

Submitted on 29 Apr 2022

**HAL** is a multi-disciplinary open access archive for the deposit and dissemination of scientific research documents, whether they are published or not. The documents may come from teaching and research institutions in France or abroad, or from public or private research centers.

L'archive ouverte pluridisciplinaire **HAL**, est destinée au dépôt et à la diffusion de documents scientifiques de niveau recherche, publiés ou non, émanant des établissements d'enseignement et de recherche français ou étrangers, des laboratoires publics ou privés.



Distributed under a Creative Commons Attribution - NonCommercial 4.0 International License

# Modified 4-Point Bending Test for Adhesion Measurement at the Interface of Iron Coated with Aluminum Casting Alloy

M. Zhe<sup>a</sup>, O. Dezellus<sup>a</sup>, G. Parry<sup>b</sup>, M. Braccini<sup>b,\*</sup> and J. C. Viala<sup>a</sup>

<sup>a</sup> Université Claude Bernard Lyon 1, LMI — UMR CNRS No 5615, 43 Bd du 11 novembre 1918, 69622 Villeurbanne Cedex, France

<sup>b</sup> Grenoble Université, SIMAP — UMR CNRS No 5266, BP 75, 38422 St Martin d'Hères Cedex, France

## Abstract

In order to reduce the weight in automotive or aeronautic components, aluminum and its alloys are being used more and more. However, their mechanical properties are not as good as those of steel and can sometimes be below the necessary requirement. To overcome this issue, reinforcement of some parts is required. In this case, the mechanical reliability of the interface between the aluminum alloy matrix and its reinforcement has to be insured. This can be done by controlling the process parameters involved in developing a strong metallurgical bond between the two metals.

In this work an Fe/Al-7 wt% Si alloy interface was investigated, aimed at linking the chemistry of the reaction layers with the toughness of the bond. First, the chemistry of the interface was characterized after immersion of Fe plates in an aluminum alloy melt. Then, the fracture energy of these assemblies was measured using a modified 4-point bending test for the adhesion measurement. In the case of pure elastic deformation during the loading, an analytical approach based on beam bending theory can be used to quantify the fracture energy. Nevertheless, in bonding between metallic partners, plastic dissipation can be expected. This is why a numerical calculation, based on a cohesive zone mode was proposed. The use of cohesive elements to describe the interface behavior allows for modeling both the threshold of de-cohesion and the progression of damage at each point of the interface.

## Keywords

Casting, fracture energy, aluminum alloys, steel, interface

## 1. Introduction

The development of multi-material systems enhances the research and understanding of the physics, chemistry and mechanics of interfaces. In particular, it is often

---

\* To whom correspondence should be addressed. Tel.: +33 4 76 82 66 88; Fax: +33 4 76 82 67 45; e-mail: [muriel.braccini@simap.grenoble-inp.fr](mailto:muriel.braccini@simap.grenoble-inp.fr)

necessary to evaluate the practical adhesion at the interfaces. Indeed, a good adhesion is a necessary condition for the interface to fulfill its function, even if it is a physical one (electrical conductivity, thermal conductivity, etc.). Various methods have been developed to mechanically characterize an interface: they either measure the strength of the interface which is the maximum load (or stress) that causes a fracture; or the interface toughness, which is the mechanical energy per unit area at which the interface separation occurs. The interface strength, measured by a tensile pull test [1], for example, is strongly dependant on crack initiation conditions. The interface toughness is measured by a steady state propagation of a crack in a fracture mechanics specimen [2–4] and provides a direct measurement of the interface adhesion energy. These kinds of methods are less sensitive to the specimen details and leads to fewer discrepancies.

The 4-point bending test is increasingly used for quantitative characterization of interface toughness [5–8] because it can be applied either to the interface between bulk materials (thick coating for example) or to thin films using a modified test where a counter-part is fixed onto the film to increase its stiffness [7]. Moreover, in the case of pure elastic deformations, the analysis is quite simple: during the crack propagation, the load is constant and depends directly on the interface adhesion energy [4]. Nevertheless, the sample preparation can sometimes be difficult, particularly when a counter-part has to be fixed because the film/counter-part interface must be stronger than the interface of interest. Moreover, pure elastic deformation hypothesis is not always fulfilled. Particularly in studies on interface between metals there is always some plastic deformation, and depending on the level of the adhesion energy and on the ductility of the metals, the plasticity will be limited to the crack tip process zone or will extend into the material. When the plastic deformation is limited to the crack tip area, the Griffith approach to brittle fracture can still be applied and the analytical relation between the toughness and the constant load is valid. In the case of an extended plasticity, the energy dissipated in the plastic deformation cannot be neglected [9]. At this point numerical methods are often used: they are based on a finite elements method in which the plastic behavior of the metals can be introduced.

One way to study interface crack propagation in finite elements methods is to introduce cohesive elements at the place of the interface. The cohesive elements are used to model cracks in homogeneous or heterogeneous materials. In the case of interface separation, this kind of approach is easier because the crack path is known and is located at the interface. As a result cohesive elements have been used in adhesive joints [10], brazing joints [11] or thin film delaminations [12]. Modeling the 4-point bending test, the cohesive elements parameters can be evaluated using an inverse method: results from the modeling are compared to experimental data. In this work this method, combining 4-point bending with cohesive zone modeling, is applied to measure the interface adhesion of a Fe/Al–Si interface. This system is of practical interest because Al–Si cast alloys are intensively used for automotive applications and their local reinforcement by ferrous inserts is a clas-

sical method to enhance their ability to sustain high load levels [13, 14]. In this case, a mechanically strong interface, ensured by a true metallurgical bond, is a key point for load transfer. Such interfaces can be obtained by means of the well-known Al-fin process which consists in two steps: aluminizing of the ferrous insert immediately followed by its insertion in a casting mould [15, 16]. This process leads to the formation of a complex interfacial reaction zone with different intermetallic phases of the ternary Al–Fe–Si system. The advanced knowledge already acquired by some of the present authors on the thermodynamic and kinetic aspects of interfacial reactivity in this ternary system [17–19] not only allows us to produce 4-point bending specimens with a rigorously controlled interfacial chemistry but also to further understand the relationship between the interfacial chemistry and mechanical properties of bimetallic systems.

## 2. Experimental

### 2.1. Materials and Procedure

Bimetallic samples were processed from an Al–7 wt% Si–0.3 wt% Mg casting alloy supplied by Alcan<sup>®</sup> and referred to as A356.2 according to ASTM standards. The composition of this alloy which will be referred to as Al–Si alloy in the present paper is given in Table 1.

Iron of commercial purity (99.5%) was provided by Goodfellow<sup>®</sup> as 1 mm thick sheets (typical composition in wt ppm: Mn 3000, Si 1000, C < 800, P < 400, S < 500, Fe balance). These sheets were cut by Electrical Discharge Machining (EDM) into plates of the desired dimension for 4-point bending test specimens: 10 mm × 60 mm. All the plates received the same surface preparation of mechanical abrasion using SiC paper under water to a mean surface roughness of about 3 μm, followed by rinsing and drying. The plates were kept in dichloromethane to prevent air contamination. A key feature to measure the toughness of an interface by 4-point bending test is to ensure that the crack propagates at the interface. In order to facilitate this interfacial propagation, some special treatment must be applied to produce a weak zone, without any metallurgical bond, at the center of the specimens. In this work this was done by depositing, just before immersion in the Al–Si alloy-melt, a thin 2 mm wide layer of Stopyt<sup>®</sup> 62A<sup>™</sup> from Wesgo<sup>®</sup> Metals

**Table 1.**

Composition (wt%) of the AlSi7Mg0.3 alloy provided by Alcan<sup>®</sup>

Element	Si	Fe	Cu	Mn	Mg	Ni	Zn	Pb + Sn	Sb	Ti	Others
Min.	6.7				0.3						
Max.	7.3	0.14	0.02	0.04	0.4	0.02	0.04	0.02	0.16	0.15	0.1
±	0.2	0.01	0.01	0.01	0.02	0.01	0.01	0.01	0.02	0.01	

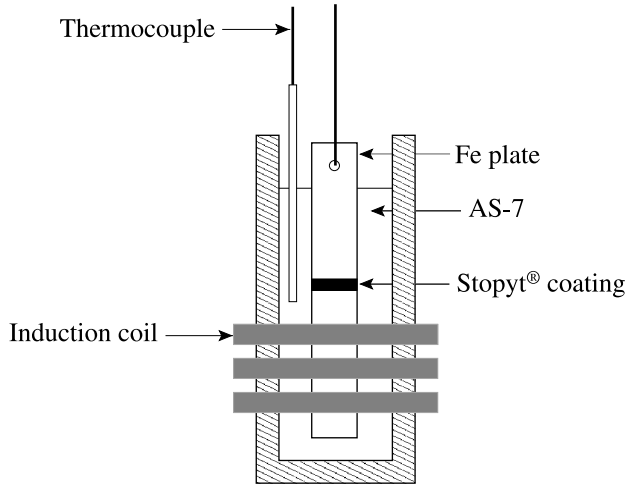


**Figure 1.** Manufacturing process of bimetallic sample by immersion of a Fe plate in a molten bath of Al–Si alloy.

(Yttrium oxide suspension in an organic liquid — a procedure often used in brazing applications to hinder the spreading of liquid metals).

The Al–Si alloy was cut into small pieces that were degreased in an ultrasonic bath of dichloromethane, placed in a ceramic oxide crucible and heated above their melting temperature by direct radio-frequency coupling as shown in Fig. 1. The establishment of a strong metallurgical bond across the liquid solid interface can be obtained only after the removal of the native oxide film layer on the Fe [20]. The removal was promoted by the dissolution of Fe in the liquid alloy and is therefore favored in the case of melts with a low Fe content [18]. However, in this case, the growth of reaction layers was limited by their dissolution in the bath until the solubility limit of Fe was reached (6–8 wt% according to [18, 21]). In the present study we have chosen to add 2 wt% Fe to the melt in order to obtain a reasonable compromise between the dissolution of Fe and the growth of the reaction layers.

Before immersion of the Fe plates the bath was regularly stirred and the surface oxide skin removed. The bath temperature was measured with a precision of better than  $\pm 0.2^\circ\text{C}$  by plunging in the melt a K-type (Ni/Cr) thermocouple. Note, that with a bath heated at  $805^\circ\text{C}$ , immersion of a Fe plate led to a temperature decrease of about  $10^\circ\text{C}$ . Therefore, interface reactions were considered to develop at a temperature of  $795 \pm 5^\circ\text{C}$ . After a 2 min of immersion, the Fe plates were gently removed from the bath and solidification of the aluminizing layer occurred in air in a few seconds.

## 2.2. Mechanical Testing

The adhesion energy of the bimetallic Al–Si alloy/Fe specimens,  $G_c$ , was measured using a 4-point bending test [4]. The test was adapted to the system of interest, which consists of a thin and brittle intermetallic layer that was enclosed between a

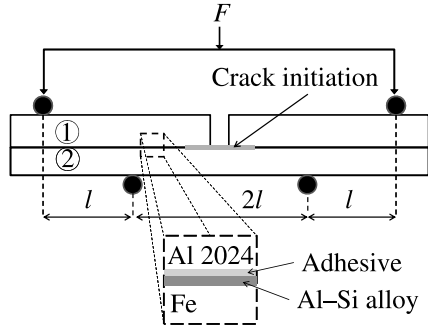


**Figure 2.** Schematic of 4-point bending test specimen with pre-notch and crack initiation.

thin aluminizing layer and the Fe sheet [7]. A metallic stiffener (Al 2024–T3) was then bonded with Araldite<sup>®</sup> 2015 on the top of the aluminized Fe plate.

During the 4-point bending test, a symmetric crack propagates along the weakest interface of the multilayer specimen. To ensure the localization of the crack at the Al–Si alloy/Fe interface, optimization of the strength of other interfaces, Al–Si alloy/Araldite<sup>®</sup> 2015 and Araldite<sup>®</sup> 2015/Al 2024, was necessary. This was done by applying a surface treatment prior to joining with the adhesive: this treatment consists of different steps including an anodization treatment step [22, 23]. Next, the aluminized Fe plate was glued to the stiffener at room temperature for 12 h in a Teflon mould in order to ensure the alignment and constant thickness of the Araldite<sup>®</sup> layer along the 4-point bending specimen. Finally, a pre-notch was made on the stiffener surface to the Fe plate using a diamond wire saw. As shown in Fig. 2, this pre-notch was located in the middle of the specimen, where a Stopyt<sup>®</sup> 62A<sup>™</sup> layer had been deposited to facilitate crack initiation in the Fe/Al–Si alloy interfacial zone.

Mechanical testing was performed in two steps: (i) initiation of a crack by 3-point bending test at a speed of 1.2 mm/min up to 1 mm displacement, (ii) followed by crack propagation by means of 4-point bending test geometry at a typical speed of 1.2 mm/min. During mechanical testing two sets of data were recorded: the classical evolution of load vs. displacement but also side view pictures of the sample were taken in order to follow the crack propagation (periodicity of 6 s).

### 2.3. Characterization

After solidification, some bimetallic specimens were cut with a diamond wire saw and diamond polished to a finish better than 1  $\mu\text{m}$  for examination by optical microscopy (OM), scanning electron microscopy (SEM) and electron probe microanalysis (EPMA). After failure in the 4-point bending test, the fracture surfaces were characterized to determine the precise path of the crack. Both sides of the fracture surface (Fe side and Al 2024 side) were observed by OM, SEM and analyzed by X-ray diffraction and EPMA. Observations were also made after failure on sections of the Fe part cut perpendicular to the fracture surface. In that case, before

mounting the sample in resin, an electroless hard Ni coating (Nicklad™ ELV 804 from MacDermid) was applied on the fracture surface in order to protect it from detrimental polishing effects such as brittle matter loss or edge rounding off.

The XRD spectra were recorded using standard diffraction equipment (Panalytical MPD-Pro diffractometer equipped with a back monochromator and a X'celerator detector, Cu  $K_\alpha$  radiation). The OM and SEM observations were made on diamond polished sections. The SEM observations and EPMA analyses were carried out using a Camebax apparatus (Cameca) equipped with an energy dispersive analyzer. The accelerating voltage was 10 kV and the beam current was 7.8 nA. After background subtraction, the counting rates obtained for Al, Fe and Si in at least eight different points were averaged and referred to the counting rates recorded under the same conditions on pure and freshly polished element standards. After corrections for atomic number, absorption and fluorescence, the atomic contents of Al, Fe and Si in the different phases deriving from the Al–Fe–Si ternary system were obtained with accuracy of better than  $\pm 0.5$  at%.

### 3. Results and Discussion

#### 3.1. Interface Chemistry

Examination by SEM of the bimetallic sample end sections indicates that the reaction zone formed at the Fe/Al–Si alloy interface, during the immersion process, consists of different intermetallic phases (see Fig. 3). More especially, the following interface reaction layer sequence was found by EPMA from Fe to Al–Si alloy: (1) a 3  $\mu\text{m}$  thick  $\eta\text{-Al}_5\text{Fe}_2(\text{Si})$  layer containing some inclusions of  $\tau_{1-9}\text{-Al}_3\text{Fe}_3\text{Si}_2$ , (2) a 2  $\mu\text{m}$  thick  $\theta\text{-Al}_{13}\text{Fe}_4(\text{Si})$  layer (3) and a 6  $\mu\text{m}$  thick  $\tau_5\text{-Al}_{7.4}\text{Fe}_2\text{Si}$  layer. According to experimental results and recent optimization of the Al–Fe–Si ternary system, the solid phase expected in equilibrium with an Al–Si alloy liquid at 795°C

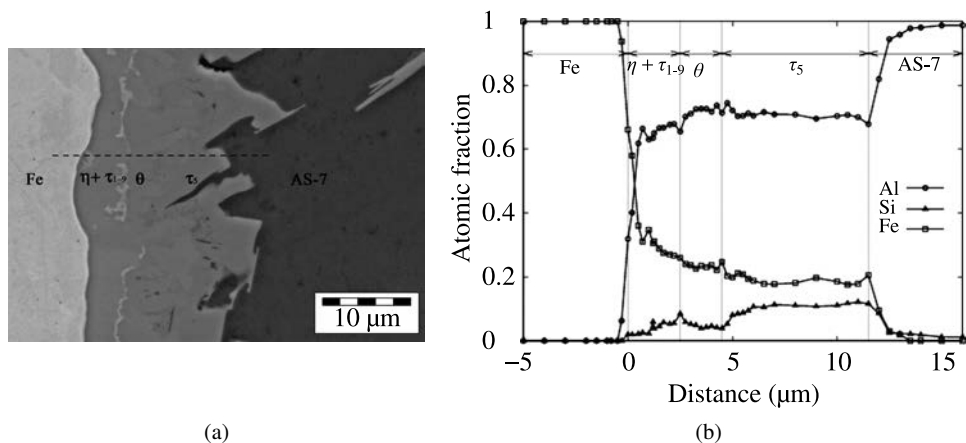


**Figure 3.** (a) Typical morphology of the interface between Fe and Al–Si alloy after 2 min of contact at 800°C. (b) EPMA concentration profiles of the Fe/Al–Si transition zone shown in (a).

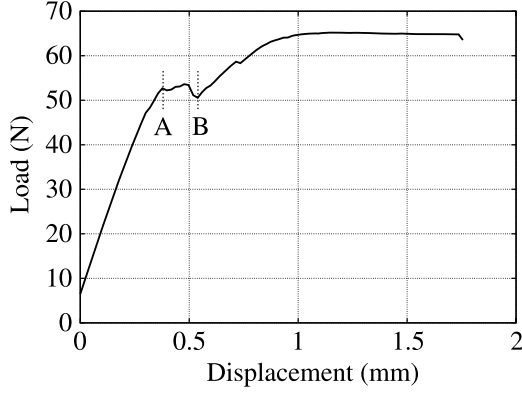


**Figure 4.** Typical load–displacement curve obtained during 4-point bending test of Al–Si alloy/Fe bimetallic specimen. Crack propagation starts at point A and ends in point B when it reaches the inner loading points (see Fig. 2).

is  $\theta$ -Al<sub>13</sub>Fe<sub>4</sub>(Si) [17, 21]. Therefore, one can conclude that the first two layers of the interfacial sequence ( $\eta$ Al<sub>5</sub>Fe<sub>2</sub>(Si) +  $\tau_{1-9}$ -Al<sub>3</sub>Fe<sub>3</sub>Si<sub>2</sub>/ $\theta$ -Al<sub>13</sub>Fe<sub>4</sub>(Si)) formed during immersion at  $795 \pm 5^\circ\text{C}$  and that this sequence corresponds to a diffusion path in the isothermal section of the ternary system at  $800^\circ\text{C}$  [18, 19]. As to the outer layer of  $\tau_5$ -Al<sub>7.4</sub>Fe<sub>2</sub>Si, it appears to have formed upon cooling as a result of Fe saturation of the liquid alloy film covering the Fe plate just removed from the bath.

### 3.2. 4-Point Bending Test

Figure 4 reports a typical load-displacement curve obtained by 4-point bending testing. Note that reproducibility has been checked by testing 7 different specimens.

Initially the load increases linearly as the sample deformed elastically. Next, a plateau was observed at a constant load level. By combining a load–displacement curve and images recording during the test, it can be concluded that during this plateau the crack propagates along the interface until it reaches the inner loading points. Finally, plasticity of the free Fe plate intervenes leading to a slow increase of the load and an important bending.

Because crack propagation occurs during elastic loading, the fracture energy of the interface  $G_c$  is equal to the strain energy release rate  $G$ , which has been established by [4] :

$$G = \frac{3 F^2 l^2 (1 - \nu_2^2)}{2 b^2 h^3 E_2} \times \left[ \frac{1}{(h_2/h)^3} - \frac{\lambda}{(h_1/h)^3 + \lambda(h_2/h)^3 + 3\lambda((h_1 h_2)/h^2)(h_1/h + \lambda(h_2/h))^{-1}} \right], \quad (1)$$

$$\text{where } \lambda = \frac{E_2}{(1-\nu_2^2)} \frac{(1-\nu_1^2)}{E_1}.$$

Subscript 1 denotes the aluminum stiffener and 2 the iron plate. Geometric parameters of these equations are the width of the specimen  $b$ , the heights of each material composing the beam  $h_1$  and  $h_2$  and the total height of the specimen  $h = h_1 + h_2$ ;  $l$  is the spacing between inner and outer load lines:  $l = 12$  mm in this study. Mechanical parameters are the elastic properties of the materials, the Young's modulus  $E$  and the Poisson's ratio  $\nu$ , and the total load  $F$ . Numerical values of those parameters are given in Table 2.

Since cracks propagate for loads between 47 N and 53 N, equation (1) gives an adhesion energy of  $23 \pm 3$  J/m<sup>2</sup>.

### 3.3. Crack Path

Results in terms of phase composition on both sides of the fracture path are illustrated by the XRD patterns presented in Fig. 5. On the Al side the diffraction lines of  $\eta$ -Al<sub>5</sub>Fe<sub>2</sub>,  $\theta$ -Al<sub>13</sub>Fe<sub>4</sub> and Al are present. Note that other phases ( $\tau_5$ -Al<sub>7.4</sub>Fe<sub>2</sub>Si and  $\tau_{1-9}$ -Al<sub>3</sub>Fe<sub>3</sub>Si<sub>2</sub>) cannot be clearly identified on this diffraction pattern because of the low intensity of the residual peaks.

On the Fe side only  $\eta$ -Al<sub>5</sub>Fe<sub>2</sub> and Fe are characterized:  $\eta$ -Al<sub>5</sub>Fe<sub>2</sub> is thus the only phase present on both sides of the crack path.

Observations on a polished section perpendicular to the Fe side complete those analyses (Fig. 6). It clearly appears in Fig. 6 that the crack has propagated in the interface reaction zone, at a distance from the  $\eta$ -Al<sub>5</sub>Fe<sub>2</sub>/Fe interface that is typically lower than 1  $\mu$ m. EPMA analyses performed at several points of the intermetallic layer remaining on Fe substrate also confirm the presence of  $\eta$ -Al<sub>5</sub>Fe<sub>2</sub> as the major phase with some Si in excess attributable to  $\tau_{1-9}$ -Al<sub>3</sub>Fe<sub>3</sub>Si<sub>2</sub> inclusions.

Combining XRD results with metallographic examination and EPMA characterization leads to the conclusion that the crack propagates in the  $\eta$ -Al<sub>5</sub>Fe<sub>2</sub> intermetallic reaction layer, most often at a distance less than 1  $\mu$ m from the Fe underlying substrate.

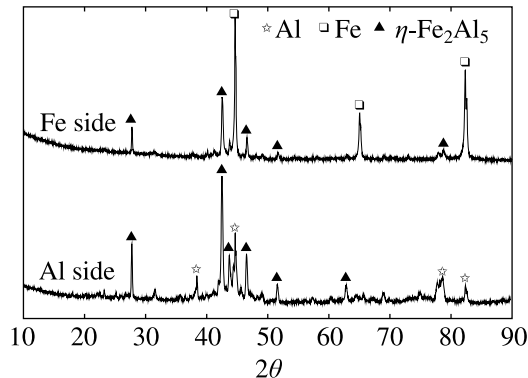


**Figure 5.** XRD pattern recorded of the fracture surfaces on both sides after 4-point bending test.

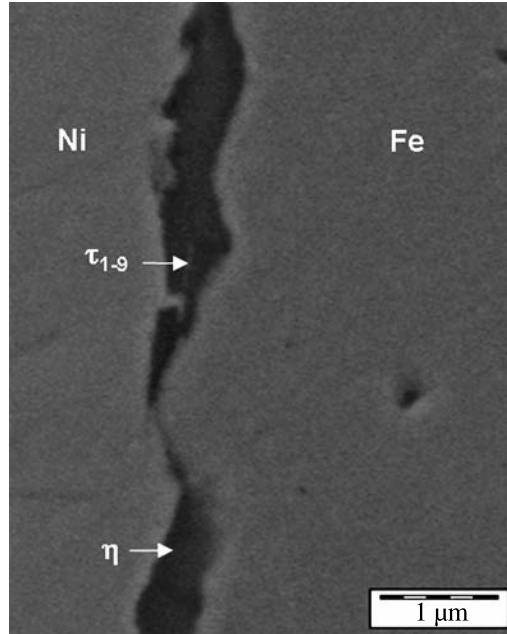


**Figure 6.** Transverse section of the fracture surface at Fe side after 4-point bending test and coating by Ni electroless plating (SEM). Phase identification has been performed by EPMA.

#### **4. Description of the Inverse Method. Application to the 4-Point Bending Test**

This section describes the numerical method that has been used in order to obtain a precise value for the toughness of the Fe/Al–Si alloy intermetallic interface, prepared as described above. Indeed the analytical approach leading to equation (1) is a simple energy balance based on elasticity calculations on the overall system. Moreover this approach omits the presence of various thin films between the two plates: reaction layers and adhesive bonds that are difficult to account for in the analytical calculation, but are readily included in the numerical calculation. Hence it is only valid for a stationary state propagation of the crack, no crack initiation or transitory crack growth can be described in this approach.

The numerical method developed here is based on cohesive zone modeling. The basic idea was to carry out a numerical simulation of the 4-point bending test, using the finite elements method involving cohesive zone elements. In these simulations, the adhesion energy is described as a local property of the interface even if it is in practice — the work of adhesion. It is possible to fit this parameter, as well as the value of the critical stress leading to the failure of the interface, by using the data from the 4-point bending experiment. If the response of the system can be numerically reproduced with enough precision on a point by point basis, then a good estimate of the interface properties can be expected.

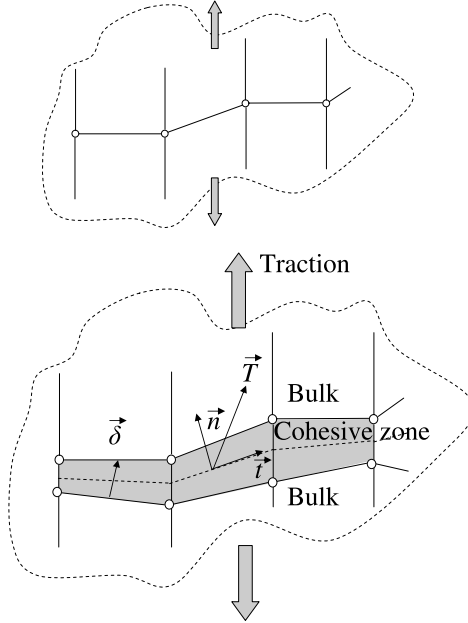


**Figure 7.** Example of a structure made of a bimaterial submitted to a remote traction. The nominal traction stress vector  $\vec{T}$ , representing the interface loading. The corresponding separation is denoted  $\vec{\delta}$ .

#### 4.1. Choice of the Cohesive Zone Model

The numerical calculations have been carried out using the finite element software ABAQUS<sup>®</sup>, in which the cohesive zone model is implemented through the use of specific elements called cohesive elements.

Cohesive zone models regard a fracture as a gradual phenomenon in which separation takes place across an extended zone in the neighborhood of the crack tip, or ‘cohesive zone’, with cohesive tractions resisting the separation. The concept of the cohesive zone used in modeling fractures, was introduced by Barenblatt [24]. Cohesive zone models became popular in the field of material sciences after the introduction of the Xu and Needleman model [25] based on an exponential cohesive law that could be conveniently introduced in finite element codes.

Cohesive zone elements implemented in finite element codes do not represent any physical material, but describe the cohesive forces which occur when material elements (such as grains) are being pulled apart: they are placed between continuum (bulk) elements, as shown in Fig. 7. The traction  $\vec{T} = T_t \vec{t} + T_n \vec{n}$  is the interface force per unit area of the interface, while the separation  $\vec{\delta} = \vec{u}_+ - \vec{u}_- = \delta_t \vec{t} + \delta_n \vec{n}$  is defined as the difference between the displacements  $\vec{u}_+$  and  $\vec{u}_-$ , respectively on the upper and the lower faces. As the calculations were carried out in the framework of plane strain, only tractions in the normal and the shear direction were considered.

When damage growth occurs these cohesive zone elements open in order to simulate crack initiation or crack growth. The description of the failure behavior is

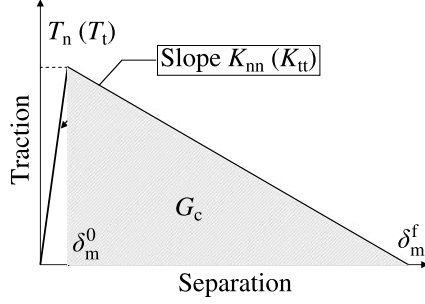


**Figure 8.** Constitutive traction separation law for the cohesive zone. The damage initiation is occurring for a given value  $\delta_m^0$  of the equivalent separation.  $\delta_m^f$  is the value of the final separation.  $G_c$  as defined in the code is the energy dissipated between  $\delta_m^0$  and  $\delta_m^f$ .

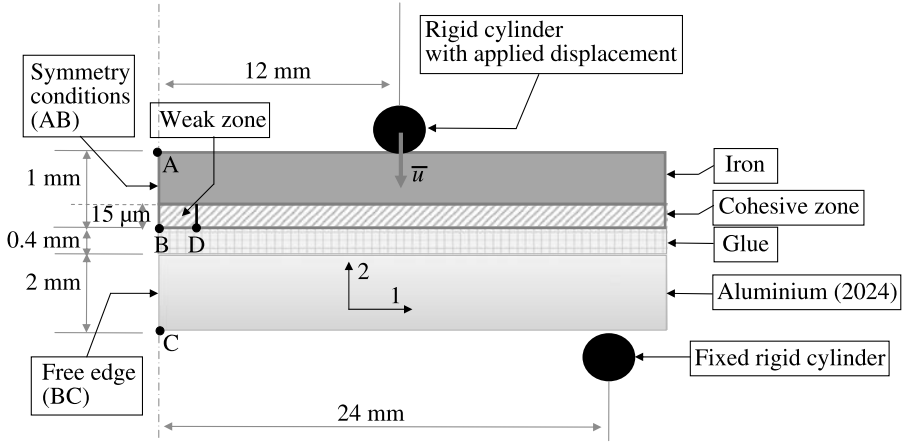


**Figure 9.** Mechanical model for the 4-point bending test of the Fe/Al 2024 specimen. Half of the model is depicted, due to symmetry. Materials and dimensions are described as well as boundary conditions.

defined by traction–separation laws. There is a great variety in traction–separation laws [26] which exhibit the same global behavior; we chose a simple bilinear law as depicted in Fig. 8 and detailed in the Appendix. As the cohesive surfaces separate, the traction first increases until a maximum is reached, and subsequently decreases to zero. The energy dissipated at failure at a material point of the interface,  $G_c$ , is given as a parameter.

#### 4.2. Application to the 4-Point Bending Test

The mechanical model used to simulate the 4-point bending test is depicted in Fig. 9. A state of plane strain is assumed (i.e., the geometry is supposed to be invariant in direction 3). The different materials composing this specimen are supposed to have an elastic behavior, except for the lower part of Fe where the damaging process is taking place: the intermetallic layers were modeled with cohesive zone

**Table 2.**

Numerical values of geometric and mechanical parameters for the 4-point bending tests

Layers	Thickness $h$ (mm)	Young's modulus $E$ (GPa)	Poisson's ratio $\nu$
Iron (subscript 2)	1	200	0.29
Al 2024 (subscript 1)	2	73	0.33
Glue	0.4	2	0.4

elements. The Young's modulus, the Poisson's ratio and the thickness of the different materials are denoted by  $E$ ,  $\nu$  and  $h$ , respectively, with an appropriate subscript.

The different layers that were taken into account are, from the top to the bottom of the multilayer: the elastic Fe layer, the cohesive zone at the bottom of Fe layer, the glue and the Al 2024 stiffener. The summary of the various layers properties can be found in Table 2. The properties chosen for the cohesive zone are discussed in the Appendix.

The aim of the numerical calculation was:

(a) to check consistency with the simple analytical approach and determine the maximal traction parameters  $T_n^0$  and  $T_t^0$  by an inverse method for a given value of  $G_c$ .

(b) To compute precisely the stresses components in the iron plate during loading in order to check the validity of the linear elasticity assumption.

The set of data generated by the numerical calculation was fitted to the corresponding set of data from the experiment in order to identify some of the parameters of the cohesive zone. The set of data was the reaction force as a function of the applied displacement of the upper loading point ( $F(\bar{u})$ ). The experimental data show that the curve  $F(\bar{u})$  was at first linear up to a given value of the applied displacement  $\bar{u}_c$ , for which the crack was beginning to propagate. Then the curve reached a short plateau  $F = F_p$ . It is worth noting that in the present case  $F_p > F(\bar{u}_c)$ , which means that the force transmitted by the loading point has to increase in order to propagate the crack. The experimental value of the plateau force  $F_p$  provides a criterion for fitting the cohesive zone parameters using the numerical results.

In order to simplify the approach, the same value was assumed for the maximal normal and shear traction components:  $T_n^0 = T_t^0 = T^0$ . The value  $G_c$  was set to  $23 \text{ J/m}^2$ , resulting from the analytical calculation carried out in Section 3. Numerical calculations have been systematically carried out with increasing values of  $T^0$ , and the results have been compared to the experimental data. The results for  $T^0 = \{30, 40, 50, 60\}$  MPa are reported in Fig. 10, together with the experimental data. The load  $F$  is plotted *versus* the applied displacement  $\bar{u}$ . Figure 10(a) shows a global view of the loading curve, whereas Fig. 10(b) focuses on the plateau. The numerical calculations produce a loading curve which is in good agreement with the experimental curve from the initial elastic regime up to the plateau. The critical displacement value  $\bar{u}_c$ , for which the response of the multilayer system becomes

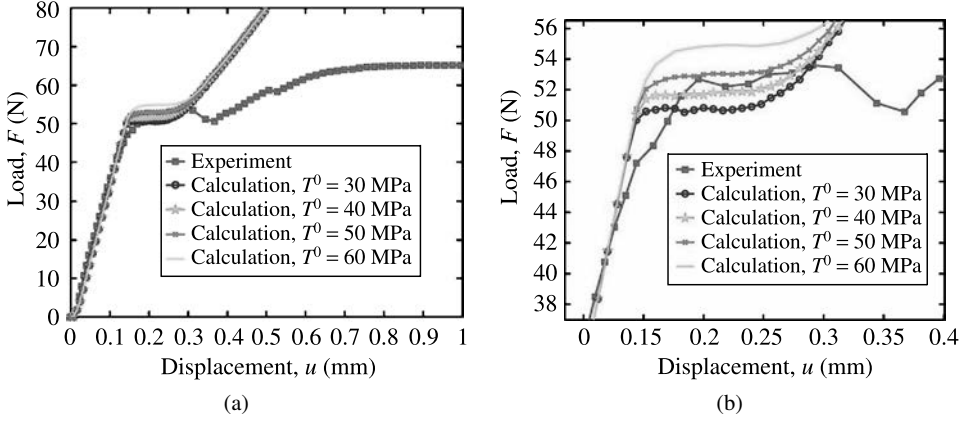


**Figure 10.** Reaction force *versus* displacement of the upper indenter, for  $G_c = 23 \text{ J/m}^2$  and various values of  $T^0$ . The evolution of the loading obtained experimentally is reported as well.

nonlinear, does not seem to be affected by the value of  $T^0$ . The best agreement is found for a maximal traction  $T^0$  between 40 and 50 MPa. It is worth noting that this value for the maximal stress  $T^0$  is quite close to some estimated in previous experimental studies on similar systems but with different testing geometries [20, 27]. However, this experimental value was indeed a value for the normal traction  $T_n^0$ . An experimental value for the shear traction would also be necessary in order to check the validity of our assumption  $T_n^0 = T_t^0 = T^0$ .

It can be concluded that the results from the finite element calculations using a cohesive zone model are quite consistent with the analytical results. The inverse method based on the comparison of the numerical and experimental output allows for the determination of a value for the maximal traction  $T^0$ .

The shapes of the numerical curve and the experimental curve are quite similar, up to the end of the plateau. However, after the plateau the two evolutions are different. This discrepancy originates in large plastic deformations occurring in the real sample in the final stage of the testing, which are not taken into account in the numerical model as it is discussed in next section.

#### 4.3. Discussion

One central assumption of both the analytical and the numerical model is that the deformations occurring in the structure are essentially elastic. It is possible to check the validity of these assumptions by analyzing the values of the stress tensor components that have been computed numerically during the loading. The evolution of the Mises stress invariant during loading has been reported in Fig. 11 for two points of the iron plate: one near the top surface and one near the bottom surface (above the cohesive zone). The experimental value of the yield stress obtained by a tensile test is also reported. These results suggest that there is no plastic deformation in the iron during the plateau, which justifies *a posteriori* the hypothesis of elastic deformations.

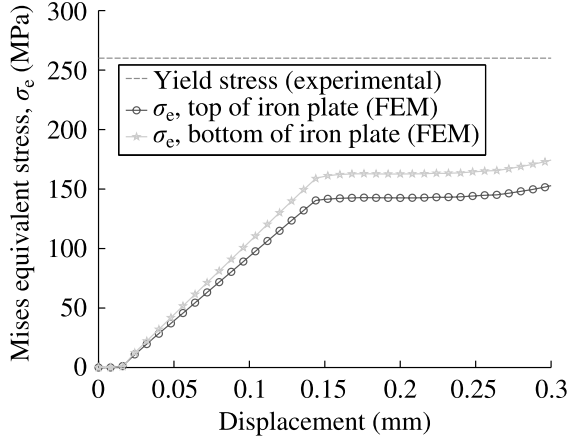


**Figure 11.** Mises equivalent stress for two points of the iron plate (one near the upper surface and one near the bottom surface) and yield stress experimentally determined by tensile test, evidencing that the deformations remain elastic up to the plateau.

The calculations also indicate that the yield stress is reached in iron for applied displacements above  $\bar{u} = 0.45$ , starting at the lower and upper surfaces of the iron layer and progressively extending to the center of the layer. This result explains why the behavior of the numerical model is so different from the one observed experimentally for larger applied displacements.

Finally, it is worth noting that in the configurations where some plasticity appears for the lower loading, no plateau was found during the experiment and the numerical approach. This was the only one to retrieve the value of  $G_c$  from experimental data. Accounting for plastic deformations in the calculation is not difficult if the plastic behavior of the material is determined by a tensile test for example (yield stress, hardening curve).

## 5. Conclusion

A modified 4-point bending test has been used to measure the fracture resistance of an Fe/Al–Si alloy interface. This interface was obtained by the immersion of Fe plates in an Al–7 wt% Si melt leading to the formation of mainly three phases in the interfacial reaction zone: a 3  $\mu\text{m}$  thick  $\eta\text{-Al}_5\text{Fe}_2(\text{Si})$  layer in contact with Fe; a 2  $\mu\text{m}$  thick  $\theta\text{-Al}_{13}\text{Fe}_4(\text{Si})$  layer and a 6  $\mu\text{m}$  thick  $\tau_5\text{-Al}_{7.4}\text{Fe}_2\text{Si}$  layer in contact with the Al–Si alloy film. Accurate characterization of the crack path by different techniques has clearly shown that crack propagates only in the  $\eta\text{Al}_5\text{Fe}_2(\text{Si})$  layer. Analytical calculation based on beam bending theory leads to a value for the fracture energy, associated with this crack growth, equal to 23  $\text{J/m}^2$ . Thus, it appears that the  $\eta\text{Al}_5\text{Fe}_2(\text{Si})$  phase is the weak layer in the interface reaction zone and should be maintained as thin as possible by controlling the solidification rate as well as during post thermal treatment.

To complete the analytical approach for 4-point bending data analysis a FEM numerical method was developed using cohesive zone modeling. An inverse method based on the comparison of numerical results to the experimental load–displacement curves allows one to calculate the interfacial properties. The cohesive zone model presented in this paper could be used for the evaluation of the interface energy in the case where the interface does not show a perfectly brittle behavior, as it is assumed in the analytical approach. One perspective would be to extend it to samples with an extended plastic deformation, i.e., when the metal surrounding the interface undergoes large plastic deformations.

### Acknowledgements

The authors like to thanks the ‘cluster MACODEV de la région Rhône-Alpes’ for funding part of this work.

### References

1. A. Kishi, S. Kurado, T. Inoue, T. Fukushima and H. Yumoto, *J. Therm. Spray Technol.* **17**, 228 (2008).
2. J. G. Williams, *Int. J. Fract.* **87**, 265 (1997).
3. J. Cognard, *J. Adhes.* **20**, 1 (1986).
4. P. G. Charalambides, J. Lund, A. G. Evans and R. M. McMeeking, *J. Appl. Mech.* **56**, 77 (1989).
5. P. Y. Thery, M. Poulain, M. Dupeux and M. Braccini, *Surf. Coat. Technol.* **202**, 648 (2007).
6. H. Li, K. A. Khor and P. Cheang, *Eng. Fract. Mech.* **74**, 1894 (2007).
7. I. Hofinger, M. Oechsner, H. A. Bahr and M. V. Swain, *Int. J. Fract.* **92**, 213 (1998).
8. R. H. Dauskart, M. Lane, Q. Ma and N. Krishna, *Eng. Fract. Mech.* **61**, 141 (1998).
9. E. Breslauer and T. Troczynski, *Mater. Sci. Eng.* **A302**, 168 (2001).
10. N. Valoroso and L. Champaney, *Eng. Fract. Mech.* **73**, 2774 (2006).
11. M. Braccini, O. Kozlova, N. Eustathopoulos, G. Parry and M.-F. Devismes, in: *Proceedings of the International Conference on Fracture XII*, Ottawa, ON, T46-001 (2009).
12. A. Shirani and K. M. Liechti, *Int. J. Fract.* **93**, 281 (1998).
13. T. W. Clyne and P. J. Withers, *An Introduction to Metal Matrix Composites*. Cambridge University Press, Cambridge (1993).
14. G. Durrant, B. Gallernault and B. Cantor, *J. Mat. Sci.* **31**, 589 (1996).
15. P. Vaillant and J. P. Petitot, *J. Phys. IV* **3**, 1853 (1993).
16. G. Gürtler, *Aluminium* **45**, 368 (1969).
17. S. Pontevecchi, F. Bosselet, F. Barbeau, M. Peronnet and J. C. Viala, *J. Phase Equilib. and Diffus.* **25**, 528 (2004).
18. J. C. Viala, M. Peronnet, F. Barbeau, F. Bosselet and J. Bouix, *Composites Part A: Appl. Sci. Manuf.* **33**, 1417 (2002).
19. D. Pierre, F. Barbeau, M. Peronnet, F. Bosselet and J. C. Viala, *Diffusion in Materials: DIMAT 2000*, Pts 1 & 2, **194-1**, 1593 (2001).
20. O. Dezellus, B. Dignonnet, M. Sacerdote-Peronnet, F. Bosselet, D. Rouby and J. C. Viala, *Int. J. Adhes. Adhes.* **27**, 417 (2007).
21. Y. Du, J. C. Schuster, Z.-K. Liu, R. Hu, P. Nash, W. Sun, W. Zhang, J. Wang, L. Zhang, C. Tang, Z. Zhu, S. Liu, Y. Ouyang, W. Zhang and N. Krendelsberger, *Intermetallics* **16**, 554 (2008).

22. D. R. Lefebvre, B. K. Ahn, D. A. Dillard and J. G. Dillard, *Int. J. Fract.* **114**, 191 (2002).
23. R. F. Wegmen, *Surface Preparation Techniques for Adhesive Bonding*. Noyes Publ., New Jersey (1990).
24. G. I. Barenblatt, *J. Appl. Math. Mech. (PMM)* **23**, 622 (1959).
25. X. P. Xu and A. Needleman, *Model. Simul. Mater. Sci. Eng.* **1**, 111 (1993).
26. N. Chandra, H. Li, C. Shet and H. Ghonem, *Int. J. Solids and Struct.* **39**, 2827 (2002).
27. O. Dezellus, L. Milani, F. Bosselet, M. Sacerdote-Peronnet, D. Rouby and J. C. Viala, *J. Mater. Sci.* **43**, 1749 (2008).

## Appendix: Boundaries Conditions and Some Details of the Numerical Model

- In the numerical approach, only half of the system was modeled, for symmetry reasons. The symmetry plane cuts the picture along the AC direction (Fig. 9). The portion BC must be set free of motion in the two directions, since a cut was made along this segment in the experimental conditions. Symmetry conditions were prescribed along AB ( $u_1 = 0$  and  $\theta_3 = 0$ , where  $u_1$  is the displacement in direction 1 and  $\theta_3$  is the rotation around direction 3). A cohesive zone thickness of 15  $\mu\text{m}$  was chosen in accordance with experimental observations.
- The two alumina rods where loading was applied were modeled as rigid cylinders. Contact conditions without friction were set up between the alumina rods and the upper and lower face of the multilayer. The lower loading point was fixed, whereas the upper one could move vertically. Hence, the experimental loading conditions were accurately reproduced. The vertical displacement of the alumina rod was prescribed during loading, and the reaction force on it could be evaluated at each step.
- Large deformations were taken into account in the simulation. The elements chosen for the glue and the Al 2024 layers were standard four nodes plane strain elements. For the Fe layer, four nodes incompatible modes plane strain elements were chosen in order to give a good representation of bending. The analysis was quasi-static.
- The traction–separation law describing the behavior of the cohesive elements at the interface between Fe and Al 2024 is depicted in Fig. 8 where  $\delta_m$  is an effective displacement define in ABAQUS<sup>®</sup> as  $\delta_m = \sqrt{\delta_n^2 + \delta_t^2}$ . It is a bilinear law. In this kind of model, the cohesive zone has a stiffness described by a stiffness matrix  $K$ , corresponding to the slope of the first linear (increasing) part of the traction/separation law before the onset of damage:

$$\vec{T} = \begin{pmatrix} T_n \\ T_t \end{pmatrix} = \begin{pmatrix} K_{nn} & K_{nt} \\ K_{nt} & K_{tt} \end{pmatrix} \begin{pmatrix} \delta_n \\ \delta_t \end{pmatrix}.$$

This stiffness is more to be seen as a numerical artifice than a real property of the interface. A quasi-rigid representation has been chosen here. The total separation work is  $\frac{\delta_m^f T^0}{2}$ ,  $\delta_m^f$  being the final separation when failure of the element is completed. The stiffness components  $K_{nn}$  and  $K_{tt}$  are chosen such that the

pseudo elastic energy (area  $\frac{\delta_m^0 T^0}{2}$  under the increasing part of the curve, where  $\delta_m^0$  is the separation corresponding to the maximum traction  $T^0$ ) is limited to 1% of the total separation work. In this condition, the total separation work can be assimilated into  $G_c$  without ambiguity.

This leads to the following values of the stiffness components:

$$K_{nn} = 100 \frac{(T_n^0)^2}{2G_c}, \quad K_{tt} = 100 \frac{(T_t^0)^2}{2G_c}, \quad K_{nt} = 0,$$

where  $T_n^0$  and  $T_t^0$  are the maximum normal (respectively shear) traction that the interface can transmit without being damaged.

The onset of damage for the interface is assumed to happen when the following equality is fulfilled:

$$\left( \frac{T_n}{T_n^0} \right)^2 + \left( \frac{T_t}{T_t^0} \right)^2 = 1.$$

From this point, damage growth in the element leads to a decrease of the stress components  $T_n$  and  $T_t$ . We chose a linear decrease according to an effective displacement define in ABAQUS<sup>®</sup> as  $\delta_m = \sqrt{\delta_n^2 + \delta_t^2}$ .

- During the specimen preparation, a weak zone was realized by the deposition of a Stopyt<sup>®</sup> 62A<sup>™</sup> layer at the center of the specimen (segment BD in Fig. 9) that opened during the preliminary 3-point bending test. The resulting crack was estimated to be 4 mm on each side. This has been taken into account in the simulations, by changing the material characteristics of the cohesive zone elements lying along this preliminary crack region of 4 mm. Very low  $T_n^0$ ,  $T_t^0$  and  $G_c$  values have been chosen for this portion of the interface. The elements along this weak line were completely damaged in the very first steps of the loading, thus initiating a 4 mm crack at the beginning of the four points bending test.
- In order to give numerical stability to the calculations, a very small viscosity coefficient has been added to the cohesive zone elements. This is a classical method that is readily implemented in ABAQUS<sup>®</sup>. Caution was taken to check that the influence of this parameter on the results was very small.